Melt Electrowriting of Liquid Crystal Elastomer Scaffolds with Programmed Mechanical Response

*Mehrzad Javadzadeh, Jesús del Barrio, and Carlos Sánchez-Somolinos**

This paper is dedicated to Prof. Mark Warner, a pioneer in LCE theory, an exceptional researcher, and an appreciated co-worker and friend.

Recently, significant advances have been achieved to precisely program the response of liquid crystal elastomers (LCEs) through extrusion-based additive manufacturing techniques; however, important challenges remain, especially when well-defined scaffolds based on ultrafine fibers are required. Here the melt electrowriting of reactive liquid crystalline inks, leading, after ultraviolet-light-induced crosslinking, to digitally positioned uniform LCE fibers with diameters ranging from hundreds of nanometers to tens of micrometers is presented, which is hardly accessible with conventional extrusion-based printing techniques. The electrowriting process induces the preferential alignment of the mesogens parallel to the fiber's axis. Such an alignment, defined by the printing path, determines the mechanical response of the crosslinked material upon stimulation. This manufacturing platform allows the preparation of open square lattice scaffolds with ultrafine fibers (a few micrometers in diameter), periods as small as 90 µm, and well-defined morphology. Additionally, the combination of accurate fiber stacking (up to 50 layers) and fiber fusion between layers leads to unprecedented microstructures composed of high-aspect-ratio LCE thin walls. The possibility of digitally controlling the printing of fibers allows the preparation complex fiber-based scaffolds with programmed and reversible shape-morphing, thus opening new avenues to prepare miniaturized actuators and smart structures for soft robotics and biomedical applications.

1. Introduction

Melt electrowriting (MEW) combines melt electrospinning (MES) principles with extrusion-based three-dimensional (3D) printing technologies to precisely position ultrafine fibers and generate polymeric microstructures.[1–5] In MEW, as in MES, a polymer melt extruded through a nozzle is electrically drawn toward a collector by using a high voltage applied between this and the nozzle, creating polymeric fibers without the need of any solvent.[6] Unlike MES, MEW introduces the computer-aided relative movement of the printhead with respect to the receiving substrate, enabling the digitally controlled positioning of the generated fibers resulting in well-defined microstructures. Compared to conventional extrusion-based digital deposition technologies, which typically produce fibers with diameters above 100 micrometers, MEW easily leads to well-positioned fibers from hundreds of nanometers to tens of micrometers.[2,3,5,7,8] Also, due to the electrostatic attraction, this technique allows precise fiber stacking leading to well-defined high walls.[1] With all these characteristics, MEW has been demonstrated to be a powerful technique for the preparation of ultrafine-fiber-based bioscaffolds with great potential in tissue engineering and regenerative medicine.[8–12]

MEW has focused primarily on the printing of thermoplastic polymers, being poly(ε-caprolactone) (PCL), with a low melting temperature and fast solidification upon cooling, the gold-standard material for this structuring technique.[1,2,13] In this case, the molten PCL is drawn as a fiber to the substrate, and it solidifies when deposited on top of the collector.[1,11,13,14] MEW

M. Javadzadeh, C. Sánchez-Somolinos
Instituto de Nanociencia y Materiales de Aragón (INMA)
CSIC-Universidad de Zaragoza
Departamento de Física de la Materia Condensada
Zaragoza 50009, Spain
E-mail: carlos.s@csic.es

The ORCID identification number(s) for the author(s) of this article can be found under https://doi.org/10.1002/adma.202209244.

J. del Barrio
Instituto de Nanociencia y Materiales de Aragón (INMA)
CSIC-Universidad de Zaragoza
Departamento de Química Orgánica
Zaragoza 50009, Spain

C. Sánchez-Somolinos
Centro de Investigación Biomédica en Red de Bioingeniería
Biomateriales y Nanomedicina
Instituto de Salud Carlos III
Zaragoza 50018, Spain

**ADVANCED
SCIENCE NEWS**

www.advancedsciencenews.com

**ADVANCED
MATERIALS**

www.advmat.de

of photocurable polymers have also been studied for which crosslinking of the deposited fiber is achieved by exposure to actinic light, allowing the preparation of robust microstructures with suitable mechanical properties for tissue engineering applications.[15,16] Recently, hydrogel materials have also been produced using MEW. Such microstructured materials can swell in a humid environment, thus introducing stimuli-responsiveness into the MEW-generated systems.[17,18] Although these so-generated scaffolds lead to significant dimensional changes, hydrogels exhibit a relatively slow response (in the orders of minutes to tens of minutes) and a limited capacity to perform mechanical work.[19] In spite of the previous examples, the MEW of stimuli-responsive polymers has been barely explored.

Liquid crystal elastomers (LCEs) are a family of lightly crosslinked liquid crystal polymer networks which are capable of undergoing large deformation in response to external stimulation (e.g., heat, light, electric fields, pH, or moisture).[20–26] Such behavior is determined by the mesogenic constituents, the polymer backbone, the degree of crosslinking, and the nature of the mesophase (e.g., nematic, smectic, etc.), among other factors.[27] Of particular importance is the preferential orientation of the mesogens constituting the LCE –defined by the director **n**– which determines the direction of the anisotropic stresses within the material and the associated deformations upon stimulation. Therefore, the microstructure of LCEs requires fine-tuning to achieve control over actuation.[28] Alignment can be imposed while processing the constituent liquid crystal molecules through various external forces, including mechanical stresses, command surfaces, and electrical or magnetic fields.[29] Recently, 3D printing methodologies based on LCE precursor extrusion-based deposition have enabled us to precisely control the morphology of the generated objects.[30–32] Digital control of the liquid crystal anisotropy is achieved through rheological alignment due to shear forces in the needle and/or elongational flow when the material is being deposited. The resulting morphology –typically fixed using photo-induced polymerization after printing– enables accurate control of the stresses and deformations generated when the 3D-printed elastomeric structure is subjected to an adequate stimulus. The combination of 3D printing technology with smart materials is unique in producing structures capable of morphing on time, a concept known as four-dimensional (4D) printing (with time being the 4th dimension).[33] Complex structures can be produced, leading to actuators with high work capacity and stimuli-responsive behavior, thus broadening the scope of LCE materials toward new soft robotic actuators and functions.[31,34,35] Fiber diameters in the range of hundreds of microns are typically achieved with this 3D printing technology; however, when fibers with diameters in the range of microns to tens of microns are needed, the processing of these structures by this type of digital-based deposition technique remains a challenge.

In this paper, we report for the first time the successful electrowriting of photopolymerizable liquid crystalline inks leading to elastomeric fibers with diameters ranging from hundreds of nanometers to tens of microns not previously achieved with other extrusion-based fabrication techniques. Advantageously, the deposited fibers exhibit a director orientation parallel to the fiber axial direction. The position of the printhead can be digitally controlled, which enables the precise deposition of fibers and, thus, the definition of the director orientation within the structure. The fibers keep their aligned morphology after photopolymerization, which leads to microstructured LCEs. Stacking these thin fibers with excellent precision has resulted in structures including square-lattice scaffolds with unparalleled small dimensions and high aspect ratio walls or porous scaffolds with more intricate designs. The built-in digitally defined anisotropy imposed during electrowriting enables the generation of fiber-based LCE scaffolds capable of reversibly deforming –in a programmed fashion– in response to external thermal stimulation. We have also demonstrated that melt electrowritten LCE scaffolds can exert mechanical forces in a pre-defined manner while performing significant mechanical work.

2. Results and Discussion

2.1. Ink Preparation

Our ink is composed of a mixture of an acrylate-terminated main-chain liquid crystal polymer and a ultraviolet (UV) photoinitiator (**Figure 1**A). The synthesis of the reactive polymer has been reported previously.[31] Such a liquid crystalline macromer was obtained by reacting 1-aminobutane with C6M via the Aza–Michael reaction. A slight excess of C6M in the Aza–Michael polymerization reaction mixture ensures that a high enough polymerization degree is achieved and that the chain ends of the polymer are equipped with acrylate groups. Such groups are involved in the UV-initiated free-radical polymerization of the liquid crystalline macromer, leading to the final crosslinked LCE scaffolds.

2.2. Electrowriting of the Ink. Fiber Formation

Electrowriting experiments using our ink were carried out using a GeSiM bioscaffolder with an electrowriting module. The setup consists of an air pressure-assisted dispensing temperature-controlled printhead with XYZ motion and a static collector. A negative voltage is applied to the collector, and the nozzle is grounded (Figure 1B). The distance between the nozzle and the collector, typically between 0.5 to 30 mm (see experimental section), is kept constant during the writing process of a single layer. During printing, the printhead is kept at 60 °C, a temperature at which the ink shows liquid crystal behavior (Figure S1, Supporting Information). Additionally, a UV lamp illuminates the collector from the top, inducing the photocrosslinking of the fibers after their deposition on top of the substrate that is placed onto the collector.

Preliminary jet initiation experiments were conducted using our ink with the described setup in static printhead conditions (Figure 1C1–4) (nozzle-to-collector distance of 30 mm). When the voltage between the collector and the nozzle was zero, no ink got through the nozzle (250 µm inner diameter) by applying pressures as high as 15 kPa. At this same pressure, however, a polymer jet is produced (Figure 1C1) when using a sufficiently high voltage (a voltage of 10 kV was employed in Figure 1C). In
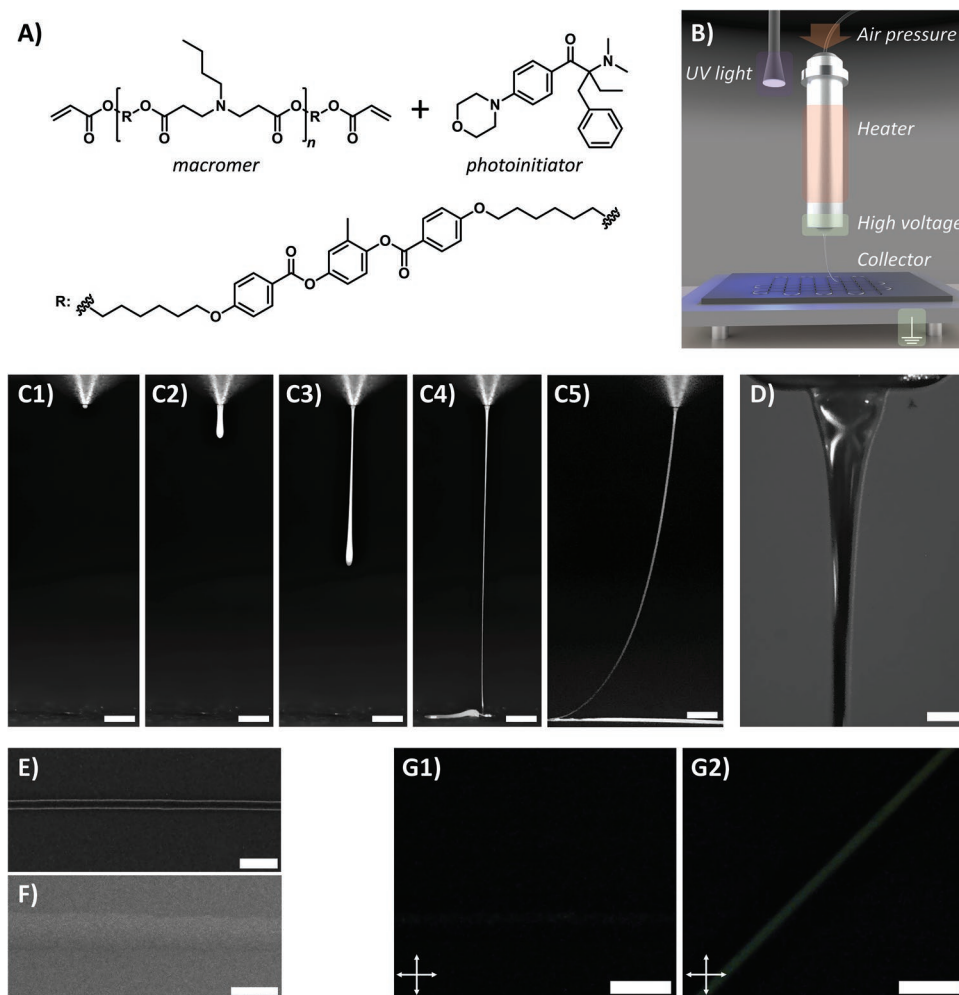
Figure 1. Melt electrowriting of LCEs: A) Ink components molecular structure. B) Schematic view of the MEW setup. A negative voltage is applied to the static collector, and the moving printhead is grounded. A UV light source cures the deposited fibers. C) Photographs after high voltage (10 kV) application (scale bar: 3 mm): C1) a rounded drop is formed in the nozzle, the drop increasing its size on time; C2) jet formation; C3) the jet is stretched, and a conical shape is formed close to the nozzle; C4) the jet is elongated, and touches the collector; C5) the printhead moves and the fiber is deposited on the substrate. D) Stabilized Taylor-cone (10 kV) (scale bar: 100 µm). E,F) SEM image of an isolated deposited straight fiber printed using a nozzle with a diameter orifice of 250 µm (scale bar: 100 µm) (E) and 100 µm (scale bar: 1 µm) (F). G) MEW polymer fibers between crossed polarizers (white arrows indicate polarizer transmission directions) (scale bar: 150 µm) with the fiber direction oriented parallel (G1) and at 45° (G2) with respect to the first polarizer transmission direction (horizontal in the pictures).

the presence of an electric field, the charges at the surface of the polymer jet generate forces that attract the polymer from the nozzle to the collector (Figure 1C1–4).[2] The jet initially rounded on account of surface tension deforms on time and adopts a conical profile (Figure 1D) at the nozzle under the high voltage effect due to the repulsive interactions between the charges of the ink.[2] The polymer jet is further drawn and elongated toward the collector (Figure 1C4), and a fine polymer fiber is eventually formed. At this point, the printhead can be moved in a controlled fashion with respect to the substrate in the XY plane while keeping a constant nozzle-to-collector distance, thus initiating the electrowriting process (Figure 1C5). The relative movement of the printhead and the collector stretches and thins the fiber, which adopts a curved shape. Once deposited, irradiation of the fibers with UV light induces the crosslinking of the liquid crystalline macromers leading to the LCE formation.

It is well known that fiber formation via MEW depends on several factors, including the nature of the ink (viscosity and charge of the ink material, for example), the environmental conditions (e.g., temperature and humidity), and the printing parameters (voltage, the pressure applied in the printhead, the relative speed between nozzle and collector, the nozzle diameter, the distance between the nozzle and the collector, etc.), among others.[2,36] Additionally, many interactions and competing forces are involved in the fiber formation process including, but not limited to, mechanical drawing, surface tension, and electric forces associated with the polymer charges; all these are highly interdependent. Therefore, it is crucial to identify how specific processing parameters affect the formation of fibers, their deposition as well as the properties of the final printed material.[2] This is even more important for a new type of ink, such as the liquid crystalline macromers investigated here.

2209244 (3 of 10)

**ADVANCED
SCIENCE NEWS**

www.advancedsciencenews.com

**ADVANCED
MATERIALS**

www.advmat.de

Initially, we explored the influence of varying the translation speed of the printhead on the deposited fiber while keeping the rest of the parameters constant (Figure S2, Supporting Information). Coiled fibers appear on the substrate at a low printhead translation speed of 1 mm s^{-1}. By increasing the printhead translation speed, sidekicks and sinusoidal meander patterns are deposited at 3 and 5 mm s^{-1}, respectively. Straight fibers are deposited at a printhead translation speed of 7 mm s^{-1}. The speed at which the velocity of the translating printhead equals that of the jet elongation, or fiber deposition velocity, is denoted as the critical translation speed (CTS).[13] Above this CTS, the deposited fibers are straight and exhibit a homogenous diameter, as shown in Figure 1E. This diameter decreases as printing speed increases, as shown in Figure S3 (Supporting Information). A nozzle translation speed larger than the fiber deposition velocity induces stretching of the fibers between the nozzle and the receiving substrate. This stretching decreases the fiber diameter, reaching values below 16 µm in the studied range of conditions. Above a ca. 20 mm s^{-1} (see Experimental Section for details), the fiber breaks, precluding the deposition of continuous controlled fibers.

In a previous work from Dalton et al.,[6] the authors predicted the relative diameter change of PCL fibers printed at different speeds above the CTS while keeping the rest of parameters constant, finding excellent agreement with experimental results. Diameters and speeds are related in their model by the Equation 1

$$D_2 = D_1 \sqrt{v_1/v_2} \qquad (1)$$

where D_1, and D_2 are the fiber diameters at speed values v_1 and v_2 respectively, being both values above the CTS. The adjustment of our experimental data to this model shows a relatively good agreement in the range of lower speeds explored, although the diameters measured at the higher speed range are smaller than those predicted by the model. The fact that fibers tend to break at speeds larger than 20 mms^{-1} could be at the origin of this deviation at high speeds (Figure S3, Supporting Information).

We have also investigated how varying the voltage affects the diameter of the printed fibers while keeping the rest of the printing parameters (Figure S4, Supporting Information). Increasing the voltage leads to deposited fibers exhibiting a smaller diameter in the studied conditions, a behavior previously found in other materials.[7,37] By observing the cone formed at the nozzle orifice (Figure S5, Supporting Information), named the "Taylor–Cone", it is possible to conclude that applying higher voltage values leads to smaller cone areas and thinner fibers, which could be attributed to the presence of higher electrostatic forces.[2] Regarding the influence of the pressure applied in the printhead on the printing process, the diameter of the fiber decreases when decreasing the applied pressure–speed, voltage, and nozzle distance are kept constant–(Figure S6, Supporting Information), which can be explained as a consequence of the lower flow rate of the ink through the nozzle.[36] As for the diameter versus speed dependency, Dalton and co-workers also predicted the relative change of fiber diameter for different pressures following Equation 2,[6]

$$D_2 = D_1 \sqrt{\frac{P_2}{P_1}} \qquad (2)$$

where D_1, and D_2 are the fiber diameters at pressure values P_1 and P_2 respectively. Our experimental data of diameter versus pressure shows in this case a good fit in the range of pressure values under study (Figure S6, Supporting Information).

Another critical parameter in MEW is the nozzle orifice diameter. We have carried out a series of experiments to investigate the performance of a nozzle with an orifice of 100 µm inner diameter –smaller in size than the 250 µm nozzle used in our initial set of experiments (vide supra)– with the idea of producing thinner fibers. Indeed, we have been capable of printing fibers with a diameter as small as 500 nm (Figure 1F). We have also found that, with our 100 µm nozzle, the trends in the variation of the fiber diameter when modifying parameters such as voltage, printing speed, and pressure are similar to those observed for the 250 µm nozzle (Figure S7, Supporting Information).

The observation of birefringence in the printed fibers was crucial to our purposes. Figures 1G1 and 1G2 present polarization optical microscopy (POM) images of a fiber deposited on a substrate at 0° (Figure 1G1) and 45° (Figure 1G2) with respect to the first polarizer transmission direction. Electrowriting experiments with ink composed of our liquid crystalline macromer and a small amount of the dichroic dye Rhodamine 700 (Figure S8, Supporting Information) showed that the liquid crystal director is preferentially aligned parallel to the axial direction of the fiber. Additional POM observations evidenced that the molecular alignment is retained after photopolymerization. Similarly to 3D printed liquid crystalline macromers, shear and elongational forces associated with the MEW process are remarkably effective at inducing the preferential orientation of the mesogenic polymer chains along the axial fiber direction. We can thus conclude that the digitally defined positioning and orientation of the printed fibers, as dictated by the movement of the printhead, enables control over the liquid crystal director morphology in the final deposited material using MEW.

2.3. Electrowriting of Square Lattice LCE Scaffolds

After achieving control over fiber deposition, we pursued the possibility of generating square lattice LCE scaffold structures by stacking layers of straight fibers. **Figure 2** shows a series of scanning electron microscopy (SEM) images of a set of square lattice scaffolds with varying spacing, number of layers, and fiber diameters. The initial sample set was produced using the 250 µm nozzle. Figure 2A shows a 300 µm period squared lattice scaffold of 4 layers per wall (4 layers at 0° and 4 layers at 90°, 8 layers at the intersection). The LCE scaffold comprises well-defined and well-positioned fibers that stack, leading to straight walls with a thickness of ≈28 µm and almost no defects. At the intersections, due to the double deposition, material accumulation takes place and fiber sagging is observed, a typical phenomenon found in MEW.[37] After deposition, the fibers are exposed to UV light, which triggers the crosslinking of the printed material. The fact that the fibers are well-defined, after printing and after UV-light exposure, evidences an adequate solidification and cross-linking of the material in our processing conditions. Remarkably, the walls show no fiber delamination due to the covalent cross-linking/fusion
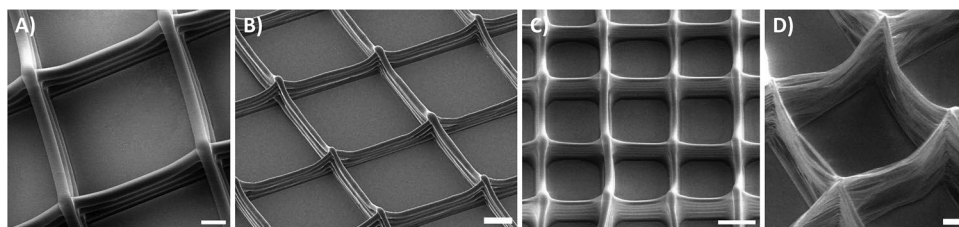
**ADVANCED
SCIENCE NEWS**

www.advancedsciencenews.com

**ADVANCED
MATERIALS**

www.advmat.de

Figure 2. Square lattice LCE scaffolds. A–D) Scanning electron microscopy images of a 300 μm-period scaffold printed with 4 layers per wall using a nozzle with a diameter orifice of 250 μm (A); a 200 μm-period square lattice scaffold of 5 layers per wall using a nozzle with a diameter orifice of 100 μm (B); a short period (90 μm) of 5 layers per wall-squared scaffold (C); and 50 layers per wall, 300 μm-period scaffold (D). Buckling observed in the thin walls might be produced by stresses generated during processing. (Scale bars: 50 μm).

between adjacent fibers at their junctions, promoting interlayer adhesion. It is also worth noting that the voltage was increased by 0.1 kV every two layers to avoid generating structural defects (breaks or gaps due to fiber bridging during the writing process appear if this voltage increase is not systematically done every two layers, as it can be seen in Figure S9, Supporting Information). As reported previously for other materials, this type of voltage modification ensures that a nearly constant electrostatic force and also an appropriate fiber stacking are achieved, as the nozzle-to-collector distance increases concurrently with the printing of subsequent layers of fibers.[38]

Using the 100 μm nozzle has enabled us to prepare square lattice scaffolds with thinner fibers. Figure 2B shows an SEM image of a 200 μm period square lattice scaffold of 5 layers per wall. MEW fibers with a diameter of only 7 μm smoothly stack during printing leading to straight vertical walls with no defects. An average height of 34 μm has been measured with SEM, nearly the thickness estimated by multiplying the number of layers by the diameter of an individual fiber (ca. 35 μm) further indicating the efficient fixation of the fiber diameter by the photopolymerization process.

To explore the fabrication of structures with smaller periods, we have prepared a 90 μm period square lattice scaffold of 5 layers per wall. Figure 2C shows an SEM image of this scaffold composed of 9 μm-thick straight vertical walls with no defects. When going to smaller periods, fiber bridging between contiguous scaffolds lines typically occurs, leading to structural defects.[39]

The number of layers constituting the scaffold can be increased by following analogous procedures to those of previous examples. Indeed, we have produced square lattice scaffolds formed by 50 layers per wall, with a 300 μm period and a fiber thickness of 7 μm (Figure 2D). Despite there are some opening defects and partial collapsing of the walls, their height, in the order of 300–400 μm, is larger than their width (300 μm) and much larger than their thickness–a series of structural features which are not achievable by conventional extrusion-based printing techniques of LCEs, thus demonstrating the potential of melt electrowriting applied to LCEs.

2.4. Electrowriting of Complex Scaffolds

MEW of predetermined curved structures is particularly challenging because of the mismatch between the programmed nozzle movement and the deposited fiber shape.[40] The main reason behind this discrepancy is the gap between the nozzle and the collector bridged by the viscoelastic jet (See Figure 1C5). In other words, the changes in the direction of the printhead are not followed by the same changes in the printed fiber pattern due to the MEW jet lag.[39] To push the limits of the MEW of liquid crystalline inks, we have investigated the preparation of more complex patterns, including curved design features. A strategy to improve the accuracy of the MEW of curved patterns relies on the minimization of jet lag. This can be achieved by reducing the printing height, i.e., working in a regime of short distance (Near Field Printing) between the nozzle and the collector, and fixing the printing movement at speed just above the CTS, minimizing the jet length and the lag.[39]

Figure 3 presents curved patterns generated by MEW of LCEs, consisting of sinusoidal structures with a hexagonal design built with microscale diameter fibers. Such porous structures have been previously proposed as membranes with tuned pore size and shape and scaffolds with tailored
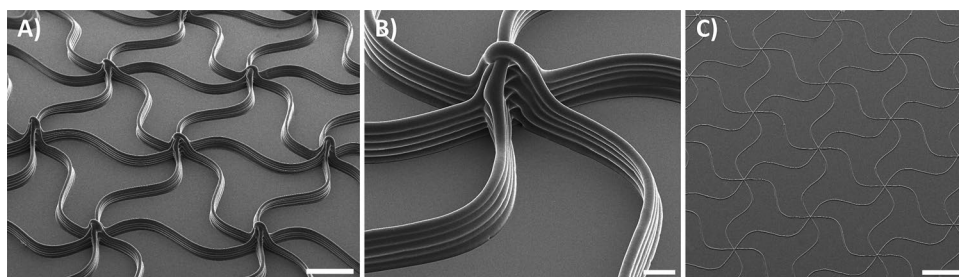

Figure 3. MEW obtained complex LCE structures. A–C) SEM images of sinusoidal fiber-based architectures with hexagonal lattice node arrangement built depositing 5 layers per wall (15 fibers at the intersection) with 60 μm-diameter fibers (A,B), and a single fiber scaffold (3 fibers at the intersection) with 16 μm-diameter fibers (C). Scale bar in (A): 1 mm; scale bar in (B): 200 μm: scale bar in (C): 500 μm.

2209244 (5 of 10)

mechanical properties capable of mimicking the mechanical behavior of specific native tissues.[31,37,41] Figure 3A,B presents a scaffold made of 5 fibers per wall having a 3 mm distance between closest fiber intersections. Accurate positioning and stacking of 60 µm-diameter fibers are demonstrated with no defects. Figure 3C presents the same design with 1 single layer of 16 µm-diameter fiber and a 950 µm distance between the closest fiber intersections. It is recognized that printing these curved structures with features smaller than those in Figure 3C remains a limitation, at least in our hands, as structural defects are frequently observed in the final structures regardless of the method chosen for MEW (Figure S10, Supporting Information). Nevertheless, our printing procedures allow for the preparation of curved fiber layers with accuracy, thus opening the doors to using liquid crystalline inks to prepare complex LCE scaffolds and porous structures.

2.5. Thermoactuation of Electrowritten Complex Scaffolds

LCEs can undergo large and controlled anisotropic shape changes in response to an external stimulus.[21] In such systems, a decrease of the mesogenic order induced, for example, by increasing the temperature, is accompanied by a contraction of the LCE along the director and an expansion along its perpendicular direction (**Figure 4**A). The possibility of exploiting MEW capability to define the liquid crystal director of the deposited fibers (as shown in Figure 1F) allows us to program the mechanical behavior of our LCE scaffolds in response to external stimulation in a similar fashion to 4D printing.[30–32] While conventional extrusion-based printing techniques allow for the controlled deposition of relatively thick fibers, MEW, in contrast, is a unique technique for producing fine fibers with diameters in the micron range and complex patterns and scaffolds (vide supra). Such features lead us to explore the potential of MEW to generate LCE ultrafine-fiber-based active microstructures with a programmed thermomechanical response.

Open pore complex periodic LCE-based MEW-generated scaffolds were initially created by depositing several layers of fibers of a uniform diameter of 60 µm, leading to walls. The structures printed over an area of 5 × 5 cm, with almost no structural defects, were produced on top of poly(vinyl alcohol) (PVA) coated glass (see experimental section). Once deposited, the material is fixed via UV-light-induced polymerization. The resulting LCE structures were released from the substrate by immersing them in water which dissolves the PVA bottom layer. The samples were mechanically attached to a metallic frame with a circular window (30 mm diameter). By carefully
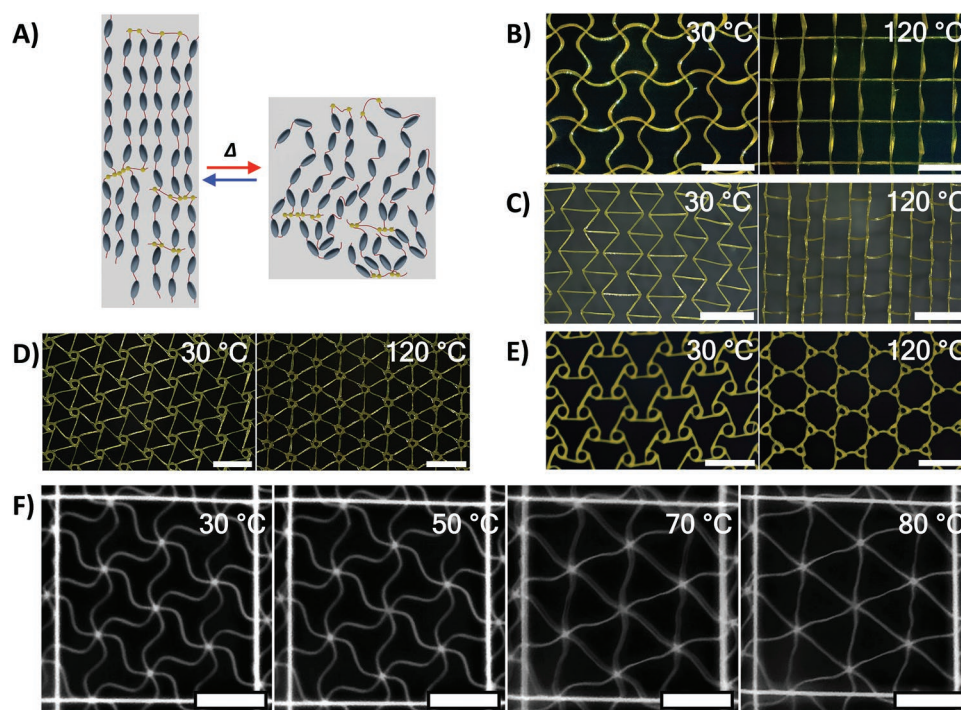

Figure 4. Thermoactuation of electrowritten LCE structures. A) Schematic representation of the thermomechanical response of uniaxially aligned LCEs. Thermally induced mesogen disorder results in contraction along the director and expansion along the orthogonal direction. B–F) Thermomechanical deformation of framed MEW LCE-based structures. B) An open pore structure formed by the arrangement of a rectangular lattice of nodes connected with sinusoidal walls, each built with 3 stacked, 60 µm-diameter fibers (scale bar: 5 mm). C) Re-entrant honeycomb structure with walls built with 4 stacked, 100 µm-diameter fibers (scale bar: 5 mm). D) Hexachiral right-handed open structure formed by a periodic array of central rings connected to its six closest neighbors by walls. The structure has 3 stacked, 70 µm-diameter fibers (scale bar: 5 mm). E) Anti-chiral open structure formed by a periodic array of central rings connected to its three closest neighbors by walls. The structure has 3 stacked, 80 µm-diameter fibers (scale bar: 5 mm). F) Open pore structure formed by the arrangement of a hexagonal lattice of nodes connected with sinusoidal walls built with a single 25 µm-diameter fiber and inter-distance of 950 µm) (scale bar: 1 mm). Unlike the rest of the experiments in this figure, thermoactuation is done underwater, instead of in the air, to keep the integrity of the ultrafine-fiber-based structure.

**ADVANCED
SCIENCE NEWS**

www.advancedsciencenews.com

**ADVANCED
MATERIALS**

www.advmat.de

performing this procedure, the final LCE specimen is attached only at the frame circumference and is free of any external stresses at room temperature (RT) except for its own weight. Figure 4B shows a 3-layer scaffold (3 fibers stacked per wall) sinusoidal fiber-based architecture with a rectangular lattice node arrangement at 30 °C. Upon heating, the fibers, with the liquid crystal director along the fiber axis, contract in this direction as described above (see Figure 4A).

Being the structure framed, this contraction of the fibers forces the walls to transition from sinusoidal at 30 °C to straight at high temperature (Figure 4B). The contraction of the fibers on heating induces the rearrangement of the structure, which at the high-temperature state shows an equally sized rectangle-based pattern. (Movie S1, Supporting Information) The fact that the nodes retain their original position evidence the homogeneity of the MEW fabricated LCE structure. The sample reverts to its original shape on cooling to 30 °C and this cycle can be repeated several times, demonstrating the reversibility of the shape-morphing behavior, as seen in Figure S11 and Movie S1 (Supporting Information).

Figure 4C shows an image corresponding to a 4 layers scaffold (4 fibers stacked per wall) based on a re-entrant honeycomb structure. It is well-known that re-entrant hexagonal honeycomb structures of conventional materials exhibit exotic mechanical behavior upon stretching as they expand in the perpendicular direction showing a negative Poisson's ratio.[42] In our case, as the scaffold is based on a responsive LCE, increasing the temperature decreases the length of the walls of the structure. As the effective length becomes shorter, the whole structure transitions from a re-entrant honeycomb structure, at 30 °C, into a rectangular pore structure at high temperature, as shown in Figure 4C.[43] The original re-entrant honeycomb structure is recovered by cooling down the sample (Movie S2, Supporting Information).

We have expanded our design strategies and explored the thermomechanical response of LCE scaffolds with chiral open structures. The basic unit cell comprises a central ring held by tangentially attached straight walls, which cannot be superimposed on its mirror image. These chiral structures can be built using a different number of connections that can be arranged in either a right- or left-handed configuration depending on the side of the wall that attaches to the central ring. Figure 4D shows a 3 layers scaffold (3 fibers stacked per wall) right-handed chiral open structure with six connections to the node. To generate each layer of this complex structure, we have sequentially deposited the material following three different printing patterns as detailed in Figure S12 (Supporting Information). As in the previous open pore structures, the chiral scaffolds were affixed to a circular metallic frame for thermoactuation studies. The linear walls contract upon heating, and the structure mutates by rotating the ring elements to release the thermally induced stresses. In our scaffold, all the rings rotate clockwise as a function of temperature while their position remains nearly fixed (Figure 4D; Movie S3, Supporting Information). Other examples of chiral open structures with three and four connections are shown in Figure S13 (Supporting Information).

In another example, we have prepared an anti-chiral structure presenting reflection symmetry. Figure 4E shows, as an example, an electrowritten 3 layers scaffold (3 fibers stacked per wall) LCE-based anti-chiral structure (printing pattern for each layer in Figure S14, Supporting Information). Upon heating, the straight walls that connect the rings contract acting in conjunction to rotate the ring either clockwise or anticlockwise, depending on the handedness of the specific connections (Figure 4E; Movie S4, Supporting Information).

We have also explored the actuation of smaller-dimension structures. Figure 4F presents a single-layer scaffold sinusoidal fiber-based architecture with the same hexagonal lattice node arrangement as in Figure 3C. Unlike the previous thicker fiber structures (Figure 4B–E), this structure, with a fiber diameter of 25 µm, was kept in water after dissolving the PVA, as these thin fibers tend to collapse when getting the sample out of our water bath due to the action of capillary forces on the fine fibers. Additionally, walls of a squared frame made of thicker LCE fibers (40 µm thick with a period of 3 mm), also seen in Figure 4F, were added to give further structural integrity to the structure. Thermoactuation of the sample was studied by heating the water to 80 °C. The supporting square lattice becomes stretched but does not change its shape, while the hexagonal lattice of fibers significantly deforms upon heating. The fibers with a sinusoidal shape at 30 °C become straight at elevated temperatures of 80 °C. Cooling down the structure reversibly gave it back to the original shape without any damage signal, demonstrating MEW's ability to digitally position LCE-based microfibers and generate complex small responsive structures hardly realizable by conventional extrusion-based printing techniques of these liquid crystalline materials.

Besides studying the ability of LCE-based MEW structures to deform into prescribed shapes, we have also explored the potential of these systems to exert relevant forces and perform mechanical work. To do this, we have prepared a spiderweb-like structure of 4 stacked fibers per wall (diameter of the fiber: 55 µm). As in the previously described cases, the LCE structure fabricated by MEW was released from the PVA-coated substrate and attached to a frame with a circular window. The framed structure, free of any stresses, is essentially undeformed at 30 °C under its own weight (**Figure 5**A), but it deforms at this same temperature when a steel ball of 16.26 g weight is placed at the center of the scaffold (Figure 5B,C). The structure is deformed by the action of gravity on the ball, and the fibers of the structure get stretched, as shown. When the temperature increases, the spiderweb LCE fibers, with the director parallel to the fiber axis, as dictated by the MEW process, contract. The contraction of the radial fibers, oriented out of the horizontal plane under the weight of the ball, makes the structure exert a net force in the upward direction (Figure 5D), which is sufficiently high to raise the ball upon heating (Figure 5B,C). The spiderweb-like structure, with a weight of 0.05 g (weight corresponding to the active region), can raise the 16.26 g steel ball, ca. 325 times its weight, a distance of 3.7 mm when heating from 30 to 120 °C (Figure 5E), demonstrating the capability of these structures to perform significant mechanical work.

3. Conclusions

We have demonstrated the controlled generation and deposition of fibers by MEW using an ink composed of a liquid

**ADVANCED
SCIENCE NEWS**

www.advancedsciencenews.com

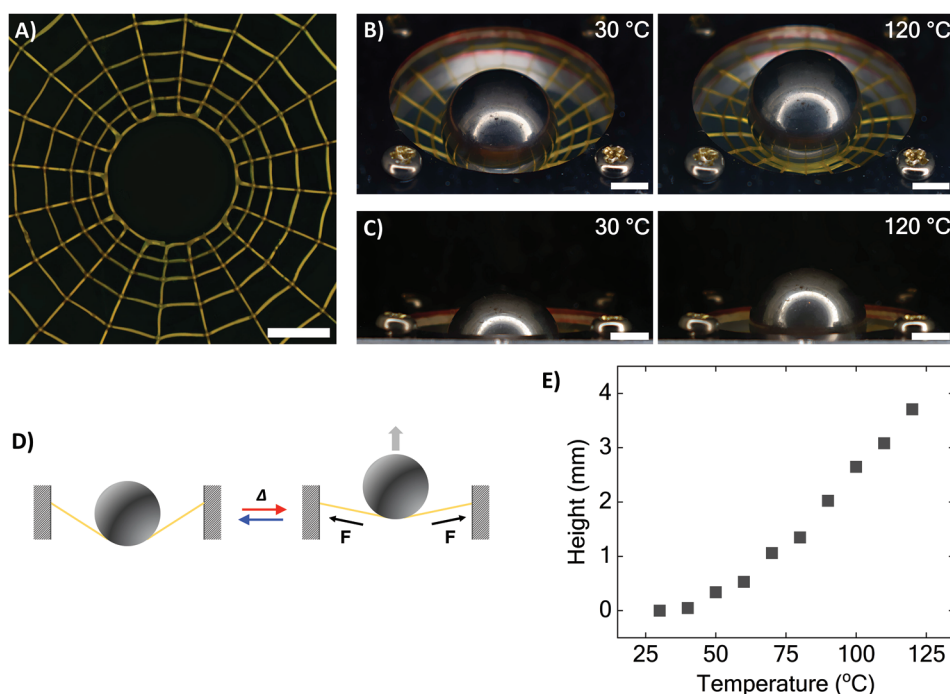**ADVANCED
MATERIALS**

www.advmat.de

Figure 5. Actuation forces by electrowritten LCE structures. A) An LCE-based MEW-fabricated spiderweb-like structure circularly framed is undeformed under its own weight at RT (scale bar: 5 mm). B,C) The structure deforms under a weight of a steel ball (16.26 g) at RT. Heating of the spiderweb-like structure raises the ball: B) oblique view and C) lateral view (scale bars: 5 mm). D) Forces exerted by the structure on the ball upon heating. The radial force components cancel out, leading to a vertical upward net force on the ball upon heating. E) Ball height as a function of temperature.

crystalline macromer and a photoinitiator. Advantageously, the liquid crystal director is aligned parallel to the axial direction of the deposited fiber, allowing the precise definition of the liquid crystal microstructure. Tuning specific processing parameters can also improve control over the fiber diameter. Our MEW methods have enabled us to print fibers with diameters ranging from hundreds of nanometers to tens of microns, much smaller than those typically obtained using conventional extrusion printing. The exposure of the fibers to UV actinic light induces the crosslinking of the reactive macromers, a process that generates LCE fibers. The so-generated anisotropic fibers present a high degree of fiber homogeneity and smoothness and good fiber stacking ability with few defects enabling the preparation of unprecedented square lattice structures with high aspect ratios and periods as small as 90 microns, pushing the limits of LCE structuring. The MEW of our liquid crystalline ink also allows the preparation, with high degree of accuracy, of complex scaffolds comprising fiber-based walls with curved geometrical features. The thermoresponsive behavior of the LCE and the control of the liquid crystal director during the writing processes allow the preparation of microfiber-based complex structures with a programmed stimuli-triggered mechanical response. In addition to the contraction of straight uniaxial fibers, the small-scale, well-defined architectures achieved using MEW evidence our ability to implement more complex motions, including localized rotations and poreshape mutations. The capability of liquid crystal melt-electrowritten scaffolds to perform a large amount of mechanical work could be effective in performing translation or rotation functions on small objects or the application of complex digitally created

force fields on adjacent material elements. Such functionalities may unlock further applications in areas including mechanobiology and tissue engineering, provided appropriate inks and stimulation procedures are developed. MEW of biocompatible materials such as PCL, has widely demonstrated to be a powerful approach to prepare complex static scaffolds that mimic structural features found in natural tissues, such as that of the myocardium.[44,45] The incorporation of stimuli-responsive LCE materials into the MEW toolbox, demonstrated in the present work, effectively leads to active biomimetic structures with digitally programmed mechanical functions. When manufactured with suitable LCE materials, these structures could serve as mechanically active biomimetic scaffolds providing, under adequate stimulation, coherent physiologically relevant strains to cells incorporated in the scaffold, mimicking in this way the cyclic mechanical forces within certain tissues (e.g., heart). These are topics that we are currently exploring in our laboratory.

4. Experimental Section

Materials: As a mesogenic unit for synthesizing the liquid crystalline macromer, a mesogenic diacrylate 1,4-bis-[4-(6-acryloyloxyhexyloxy) benzoyloxy]-2-methylbenzene, usually referred to as RM82 or C6M was used, that was obtained from Synthon Chemicals. As a chain extender, n-butylamine, purchased from Aldrich was chosen. The photoinitiator 2-benzyl-2-(dimethylamine)-4′-morpholinobutyrophenone, also called Irgacure 369, was obtained from Aldrich. Tetrahydrofuran (THF), used as a solvent for the Michael addition reaction, was purchased from Aldrich. PVA was also purchased from Aldrich, 80% hydrolyzed, with

2209244 (8 of 10)

Mw 9000–10 000, and used as a temporary layer to release the printed structures.

Ink Preparation: The amine and the reactive monomer were added to an amber flask in a 1:1.01 molar ratio. Above this, 2 wt% of photoinitiator was added to the mixture. THF was added as a solvent for the reaction, in the same weight as the total reactants content. The solution was homogenized using a magnetic stirrer and allowed to react for 24 h at 70 °C in an open flask. After 24 h, to be sure of releasing all the additional THF, the sample was kept in a vacuum oven for 72 h under mild vacuum conditions (100 mbar). Finally, the sample recovered the initial weight, before THF addition, within less than 1 wt%.

MEW Device: A Bio-Scaffolder (Bio-Scaffolder 3.1, GeSiM GmbH, Großerkmannsdorf, Germany) with a melt electrospinning module (GeSiM, Germany) was used for MEW of lines and scaffolds. The Bio-Scaffolder was equipped with high precision X–Y–Z linear axes, a pressure and temperature-controlled stainless-steel cartridge (10 mL) provided with a conic nozzle (250 or 100 µm nozzle orifice diameter). A negative-channel voltage generator was used to apply the desired voltage to the collector while the printhead was grounded. The internal equipment software set the processing parameters (pressure, temperature, and printing speed).

Scaffolds Designing Files: Single lines were generated with "Scaffold Generator (SG)" software (GeSiM GmbH, 2021 software). For the rest of the scaffolds, G-Code commands were initially generated using CAD fusion software from Aerotech Inc. Modifications of the code for a correct interface with the Bio-Scaffolder router were done manually. The generated code for each pattern was finally imported to the Bio-Scaffolder.

Electrowriting of LCE Structures: Cartridges were filled with the ink, and the temperature was set to 60 °C for 3 h before printing to facilitate removing bubbles from the ink. The printhead temperature was set at 60 °C while the receiving substrate was kept at RT to help printed line stabilization. MEW protocols were developed by optimizing printing parameters such as printing speed (*s*): 0.65 to 20 mm s^{-1}; extrusion pressure (*P*): 1 to 15 kPa; voltage (*V*):-(2.5 to 16 kV), tip to collector distance (Z-Offset): nominal distance in the printer software was selected between 0.5 to 30 mm; however it is essential to mention that, the reference height of the nozzle tip (*Z* = 0 mm) was fixed by default at 1.13 mm distance to the tray for safety reasons. Fibers were directly written onto ultrathin glass microscope slides (with a thickness of 0.13 mm), except for those samples to be released (shape-morphing samples) printed on top of 50 × 50 mm, 1.1 mm-thick indium tin oxide (ITO) glasses with a 150 nm PVA layer deposited on top. Before printing, glass slides were cleaned with isopropanol in an ultrasound bath for 10 min and dried before use. The printing tip and substrate separation were maintained constant during the printing of each layer. It is important to mention that the voltage was increased by 0.1 kV every two layers to avoid the formation of structural defects (breaks or gaps due to fiber bridging during the writing process). Just after fiber deposition, an EXFO UV lamp (320 to 390 nm, 10 mW cm^{-2}) was used to irradiate directly from the top of the printing area to crosslink and stabilize the situated fiber. After printing the last layer, the samples were irradiated in two steps: i) kept under the same lamp at RT for 5 min, and ii) irradiated under UV irradiation (Thorlabs 365 nm LED–100 mW cm^{-2}) for 20 more minutes.

SEM Analysis: SEM analysis was performed using a QUANTA-FEG250 (FEI) at 10 kV under low vacuum, without coating the sample, and an Inspect F50 (FEI) at 10 kV with a coating of 14 nm under a high-vacuum environment.

POM Analysis: The structures were examined using a Nikon Eclipse 80I POM.

Thermoactuation Experiments: Free-standing samples were prepared for morphing experiments (Figures 4 and 5, except for Figure 4F). Scaffolds were deposited on PVA-coated ITO-glass substrates. These were prepared by applying a 5 wt% PVA solution in Milli-Q water by spin coating using a first spinning cycle at 25 rpm for 12 s followed by a second one of 50 rpm for 3 s and then dried at 70 °C for 1 h. After printing and curing, the structures were first fixed to an aluminum frame having a circular window (30 mm diameter) using waterproof adhesive.

The sample and the frame were immersed in water to dissolve the PVA. After a few hours, the structure was released from the glass plate. The MEW structure was further mechanically fixed to the initial frame by using a second similar aluminum frame provided with suitable screws that exert pressure on the sample at the frame region. The thermoactuation and shape recovery experiments were conducted in the air using a homemade aluminum oven cavity with a glass cover that allowed deformation observation. The samples were fixed inside the oven cavity, and the temperature was monitored using a thermocouple placed close to the sample. Thermoactuation experiments with fine fiber-based scaffolds (Figure 4F) were performed in Milli-Q water. In this case, the sample was framed using a similar procedure described above. Once it was immersed in water to dissolve the PVA, the sample was kept under water where actuation experiments were performed. In all the cases, actuation was monitored using a digital camera Nikon D5200 and image analysis using ImageJ.

Supporting Information

Supporting Information is available from the Wiley Online Library or from the author.

Conflict of Interest

The authors declare no conflict of interest.

Data Availability Statement

Data will be available in Zenodo repository upon publication.

**ADVANCED
SCIENCE NEWS**
www.advancedsciencenews.com

**ADVANCED
MATERIALS**
www.advmat.de

[1]   T. D. Brown, P. D. Dalton, D. W. Hutmacher, *Adv. Mater.* **2011**, *23*, 5651.

[2]   T. D. Brown, P. D. Dalton, D. W. Hutmacher, *Prog. Polym. Sci.* **2016**, *56*, 116.

[3]   P. Mieszczanek, T. M. Robinson, P. D. Dalton, D. W. Hutmacher, *Adv. Mater.* **2021**, *33*, 2100519.

[4]   J. C. Kade, P. D. Dalton, *Adv. Healthcare Mater.* **2021**, *10*, 2001232.

[5]   H. Haag, P. D. Dalton, V. Bloemen, *Adv. Funct. Mater.* **2022**, *32*, 2201414.

[6]   A. Hrynevich, B. Ş. Elçi, J. N. Haigh, R. McMaster, A. Youssef, C. Blum, T. Blunk, G. Hochleitner, J. Groll, P. D. Dalton, *Small* **2018**, *14*, 1800232.

[7]   M. Castilho, D. Feyen, M. Flandes-Iparraguirre, G. Hochleitner, J. Groll, P. A. F. Doevendans, T. Vermonden, K. Ito, J. P. G. Sluijter, J. Malda, *Adv. Healthcare Mater.* **2017**, *6*, 1700311.

[8]   I. Liashenko, A. Hrynevich, P. D. Dalton, *Adv. Mater.* **2020**, *32*, 2001874.

[9]   E. Hewitt, S. Mros, M. Mcconnell, J. Cabral, A. Ali, *Biomed. Mater.* **2019**, *14*, 055013.

[10] E. Bakirci, N. Schaefer, O. Dahri, A. Hrynevich, P. Strissel, R. Strick, P. D. Dalton, C. Villmann, *Adv. Biosyst.* **2020**, *4*, 2000077.

[11] M. von Witzleben, T. Stoppe, T. Ahlfeld, A. Bernhardt, M. Polk, M. Bornitz, M. Neudert, M. Gelinsky, *Adv. Healthcare Mater.* **2021**, *10*, 2002089.

[12] M. T. Ross, D. Kilian, A. Lode, J. Ren, M. C. Allenby, M. Gelinsky, M. A. Woodruff, *Int. J. Bioprint.* **2021**, *23*, 00158.

[13] G. Hochleitner, A. Youssef, A. Hrynevich, J. N. Haigh, T. Jungst, J. Groll, P. D. Dalton, *BioNanomaterials* **2016**, *17*, 159.

[14] G. Hochleitner, E. Fürsattel, R. Giesa, J. Groll, H. - W. Schmidt, P. D. Dalton, *Macromol. Rapid Commun.* **2018**, *39*, 1800055.

[15] F. Chen, G. Hochleitner, T. Woodfield, J. Groll, P. D. Dalton, B. G. Amsden, *Biomacromolecules* **2016**, *17*, 208.

[16] G. Hochleitner, F. Chen, C. Blum, P. D. Dalton, B. Amsden, J. Groll, *Acta Biomater.* **2018**, *72*, 110.

[17] D. J. Wu, N. H. Vonk, B. A. G. Lamers, M. Castilho, J. Malda, J. P. M. Hoefnagels, P. Y. W. Dankers, *Eur. Polym. J.* **2020**, *141*, 110099.

[18] D. Nahm, F. Weigl, N. Schaefer, A. Sancho, A. Frank, J. Groll, C. Villmann, H.-W. Schmidt, P. D. Dalton, R. Luxenhofer, *Mater. Horiz.* **2020**, *7*, 928.

[19] A. Sydney Gladman, E. A. Matsumoto, R. G. Nuzzo, L. Mahadevan, J. A. Lewis, *Nat. Mater.* **2016**, *15*, 413.

[20] A. Greiner, *Macromol. Rapid Commun.* **2005**, *26*, 1361.

[21] D. J. Broer, G. N. Mol, *Polym. Eng. Sci.* **1991**, *31*, 625.

[22] J. Naciri, A. Srinivasan, H. Jeon, N. Nikolov, P. Keller, B. R. Ratna, *Macromolecules* **2003**, *36*, 8499.

[23] Y. Yu, M. Nakano, T. Ikeda, *Nature* **2003**, *425*, 145.

[24] K. D. Harris, C. W. M. Bastiaansen, J. Lub, D. J. Broer, *Nano Lett.* **2005**, *5*, 1857.

[25] D. J. Broer, *Adv. Mater.* **2020**, *32*, 1905144.

[26] T. J. White, D. J. Broer, *Nat. Mater.* **2015**, *14*, 1087.

[27] D. Broer, G. P. Crawford, S. Zumer, *Cross-Linked Liquid Crystalline Systems*, CRC Press, Boca Raton, FL, USA **2011**.

[28] M. Warner, *Annu. Rev. Condens. Matter Phys.* **2020**, *11*, 125.

[29] K. M. Herbert, H. E. Fowler, J. M. McCracken, K. R. Schlafmann, J. A. Koch, T. J. White, *Nat. Rev. Mater.* **2022**, *7*, 23.

[30] C. P. Ambulo, J. J. Burroughs, J. M. Boothby, H. Kim, M. R. Shankar, T. H. Ware, *ACS Appl. Mater. Interfaces* **2017**, *9*, 37332.

[31] M. López-Valdeolivas, D. Liu, D. J. Broer, C. Sánchez-Somolinos, *Macromol. Rapid Commun.* **2018**, *39*, 1700710.

[32] A. Kotikian, R. L. Truby, J. W. Boley, T. J. White, J. A. Lewis, *Adv. Mater.* **2018**, *30*, 1706164.

[33] S. Tibbits, *Archit. Des.* **2014**, *84*, 116.

[34] A. Kotikian, C. McMahan, E. C. Davidson, J. M. Muhammad, R. D. Weeks, C. Daraio, J. A. Lewis, *Sci. Rob.* **2019**, *4*, aax7044.

[35] L. Ceamanos, Z. Kahveci, M. López-Valdeolivas, D. Liu, D. J. Broer, C. Sánchez-Somolinos, *ACS Appl. Mater. Interfaces* **2020**, *12*, 44195.

[36] F. M. Wunner, P. Mieszczanek, O. Bas, S. Eggert, J. Maartens, P. D. Dalton, E. M. De-Juan-Pardo, D. W. Hutmacher, *Biofabrication* **2019**, *11*, 025004.

[37] T. M. Robinson, D. W. Hutmacher, P. D. Dalton, *Adv. Funct. Mater.* **2019**, *29*, 1904664.

[38] F. M. Wunner, M. Wille, T. G. Noonan, O. Bas, P. D. Dalton, E. M. De-Juan-Pardo, D. W. Hutmacher, *Adv. Mater.* **2018**, *30*, 1706570.

[39] J. Kim, E. Bakirci, K. L. O'Neill, A. Hrynevich, P. D. Dalton, *Macromol. Mater. Eng.* **2021**, *306*, 2000685.

[40] A. Hrynevich, I. Liashenko, P. D. Dalton, *Adv. Mater. Technol.* **2020**, *5*, 2000772.

[41] O. Bas, D. D'Angella, J. G. Baldwin, N. J. Castro, F. M. Wunner, N. T. Saidy, S. Kollmannsberger, A. Reali, E. Rank, E. M. De-Juan-Pardo, D. W. Hutmacher, *ACS Appl. Mater. Interfaces* **2017**, *9*, 29430.

[42] I. G. Masters, K. E. Evans, *Compos. Struct.* **1996**, *35*, 403.

[43] L. Yang, O. Harrysson, H. West, D. Cormier, *Int. J. Solids Struct.* **2015**, *69–70*, 475.

[44] M. Castilho, A. van Mil, M. Maher, C. H. G. Metz, G. Hochleitner, J. Groll, P. A. Doevendans, K. Ito, J. P. G. Sluijter, J. Malda, *Adv. Funct. Mater.* **2018**, *28*, 1803151.

[45] N. T. Saidy, T. Shabab, O. Bas, D. M. Rojas-González, M. Menne, T. Henry, D. W. Hutmacher, P. Mela, E. M. De-Juan-Pardo, *Front Bioeng. Biotechnol.* **2020**, *8*, 793.